Magnetic Resonance in Medicine

3D Free-breathing multichannel absolute B_1^+ Mapping in the human body at 7T

Sebastian Dietrich[1] | Christoph S. Aigner[1] | Christoph Kolbitsch[1] | Johannes Mayer[1] | Juliane Ludwig[1] | Simon Schmidt[2] | Tobias Schaeffter[1,3] | Sebastian Schmitter[1,2,4]

[1]Physikalisch-Technische Bundesanstalt (PTB), Braunschweig and Berlin, Germany

[2]Medical Physics in Radiology, German Cancer Research Center (DKFZ), Heidelberg, Germany

[3]Department of Medical Engineering, Technische Universität Berlin, Berlin, Germany

[4]Center for Magnetic Resonance Research, University of Minnesota, Minneapolis, Minnesota, USA

Correspondence
Sebastian Schmitter, Physikalisch-Technische Bundesanstalt (PTB), Brauschweig and Berlin, Abbestraße 2–12, 10587 Berlin, Germany.
Email: sebastian.schmitter@ptb.de

Purpose: To introduce and investigate a method for free-breathing three-dimensional (3D) B_1^+ mapping of the human body at ultrahigh field (UHF), which can be used to generate homogenous flip angle (FA) distributions in the human body at UHF.

Methods: A 3D relative B_1^+ mapping sequence with a radial phase-encoding (RPE) k-space trajectory was developed and applied in 11 healthy subjects at 7T. An RPE-based actual flip angle mapping method was applied with a dedicated B_1^+ shim setting to calibrate the relative B_1^+ maps yielding absolute B_1^+ maps of the individual transmit channels. The method was evaluated in a motion phantom and by multidimensional in vivo measurements. Additionally, 3D gradient echo scans with and without static phase-only B_1^+ shims were used to qualitatively validate B_1^+ shim predictions.

Results: The phantom validation revealed good agreement for B_1^+ maps between dynamic measurement and static reference acquisition. The proposed 3D method was successfully validated in vivo by comparing magnitude and phase distributions with a 2D Cartesian reference. 3D B_1^+ maps free from visible motion artifacts were successfully acquired for 11 subjects with body mass indexes ranging from 19 kg/m^2 to 34 kg/m^2. 3D respiration-resolved absolute B_1^+ maps indicated FA differences between inhalation and exhalation up to 15% for one channel and up to 24% for combined channels for shallow breathing.

Conclusion: The proposed method provides respiration-resolved absolute 3D B_1^+ maps of the human body at UHF, which enables the investigation and development of 3D B_1^+ shimming and parallel transmission methods to further enhance body imaging at UHF.

KEYWORDS
7 Tesla, actual flip angle imaging, body imaging, B_1^+ mapping, radial phase encoding, ultrahigh field

1 | INTRODUCTION

One of the major challenges at ultrahigh magnetic field (UHF) is the heterogeneous amplitude of the transmit (Tx) magnetic field (B_1^+). It yields a spatially heterogeneous flip angle (FA) and, therefore, spatially varying contrast-limiting UHF applications. This issue has been addressed, among other solutions, using multitransmit coils in combination with several different parallel transmission (pTx) strategies.[1,2]

Several studies have also demonstrated that pTx methods strongly improve signal-to-noise and contrast-to-noise ratios when targeting the human body.[3] Moreover, FA variations in the human body are typically more pronounced than in the human brain because of the larger and patient-dependent body size. Static pTx methods are often sufficient to achieve acceptable FA homogeneity for small two-dimensional (2D) regions of interest (ROIs) such as used for the prostate,[4] whereas the complexity of the pTx strategies needs to increase when large organs such as the liver[5] are targeted. Therefore, it is expected that an extension of the ROI to cover a larger 3D volume in the human body also requires more complex FA optimization strategies.

The knowledge of the underlying B_1^+ maps of each single Tx channel is a prerequisite for any pTx optimization, independent of the target region. Such maps are either acquired for each subject at the beginning of each session or in case of universal pulses[6] during a set of training subjects, which then eliminates the need for subject-specific B_1^+ mapping. Several different techniques for acquiring (absolute) B_1^+ maps exist, among them are methods based on the Bloch-Siegert shift,[7] presaturation turbo fast low-angle shot,[8] dual refocusing echo acquisition (DREAM),[9,10] and actual flip angle imaging (AFI).[11] A straightforward approach to obtain individual B_1^+ maps of each Tx channel consists of combining a single absolute B_1^+ map obtained by one of the aforementioned methods[7–9,11] with a set of multiple Tx gradient echo (GRE) acquisitions, where, for example, only a single Tx channel is active per acquisition.[12] Similarly, absolute 2D B_1^+ maps can also be acquired based on the B1TIAMO method.[13]

For obtaining absolute B_1^+ maps in the human body at 7T of multiple 2D slices or 3D volumes, however, the aforementioned methods are often limited by radiofrequency (RF) power demand, motion, and/or blood flow and their acquisition times might be too long for a breath-hold. Instead, a method for generating relative B_1^+ estimations[14] of the N_{Tx} Tx channels, initially introduced for the human brain, can be acquired without high power requirements based on GRE images with low FAs. This allows the acquisition of B_1^+ maps of a single slice within a few seconds, that is, within a breath-hold when applied to the body. However, a limitation of this method is that the amplitude of the maps is relative, if no additional absolute B_1^+ map is acquired to calibrate these maps, and that the maps are biased by the square-root of the proton density.[14] Despite these limitations, the relative B_1^+ mapping method has proven to be highly suitable for FA optimization in the human body at 7T, not only for B_1^+ shimming purposes,[15,16] but also for slice-selective pTx methods such as spokes RF pulses.[5,17,18] For pTx techniques that optimize the FA within 3D volumes such as the whole liver or heart, however, B_1^+ maps covering the 3D volume are required. Although the relative B_1^+ mapping technique mentioned previously has been extended to multiple slices,[17,19] full 3D mapping cannot be achieved within a single breath-hold.

Therefore, we investigate in this work a method to acquire free-breathing, 3D absolute B_1^+ maps in the human body at 7T.[20] This technique is based on a fast, low-power–demanding relative B_1^+ mapping method,[14] as well as a radial phase-encoding (RPE) acquisition scheme,[21–23] which enables retrospective binning in respiratory motion states. This flexible 3D acquisition scheme is applied for two acquisitions: (1) a modified AFI calibration scan to acquire absolute B_1^+ maps in a combined, single Tx configuration[24]; and (2) small FA spoiled GRE acquisitions. We first use the GRE scans to derive relative B_1^+ maps of the human body that are subsequently calibrated using the AFI scan resulting in estimated, absolute B_1^+ maps of each channel and different respiratory motion states. We quantitatively evaluate the method first in a motion phantom scan and subsequently show the suitability of this technique to compute B_1^+ maps in 11 volunteers. 2D Cartesian cine GRE scans, as well as 3D GRE scans with and without static phase-only B_1^+ shims are used to qualitatively validate the resulting B_1^+ maps.

2 | METHODS

Our method to compute multichannel 3D respiration-resolved, absolute B_1^+ estimations relies on two separate acquisitions: an RPE-based, 3D respiration-resolved AFI (RPE-AFI) acquisition,[24] and a Tx channel-wise RPE-based[23,25] 3D respiration-resolved-gradient echo (Tx-RPE-GRE) acquisition. An overview of the workflow is depicted in Figure 1A. Relative B_1^+ maps are calculated from Tx-RPE-GRE and calibrated with RPE-AFI to obtain absolute B_1^+ map estimations. To obtain a sufficiently high FA for the calibration, the RPE-AFI is measured with a B_1^+ shim setting Φ_{eff}, providing a locally high Tx efficiency in the frontal region of the heart. Calibration is then performed for ROIs in the heart with a FA > 40° (see the white ROI in Figure 1A).

2.1 | Radial phase encoding and self-navigation

Using an RPE-based acquisition, respiration-resolved images are obtained by acquiring the 3D k-space as illustrated
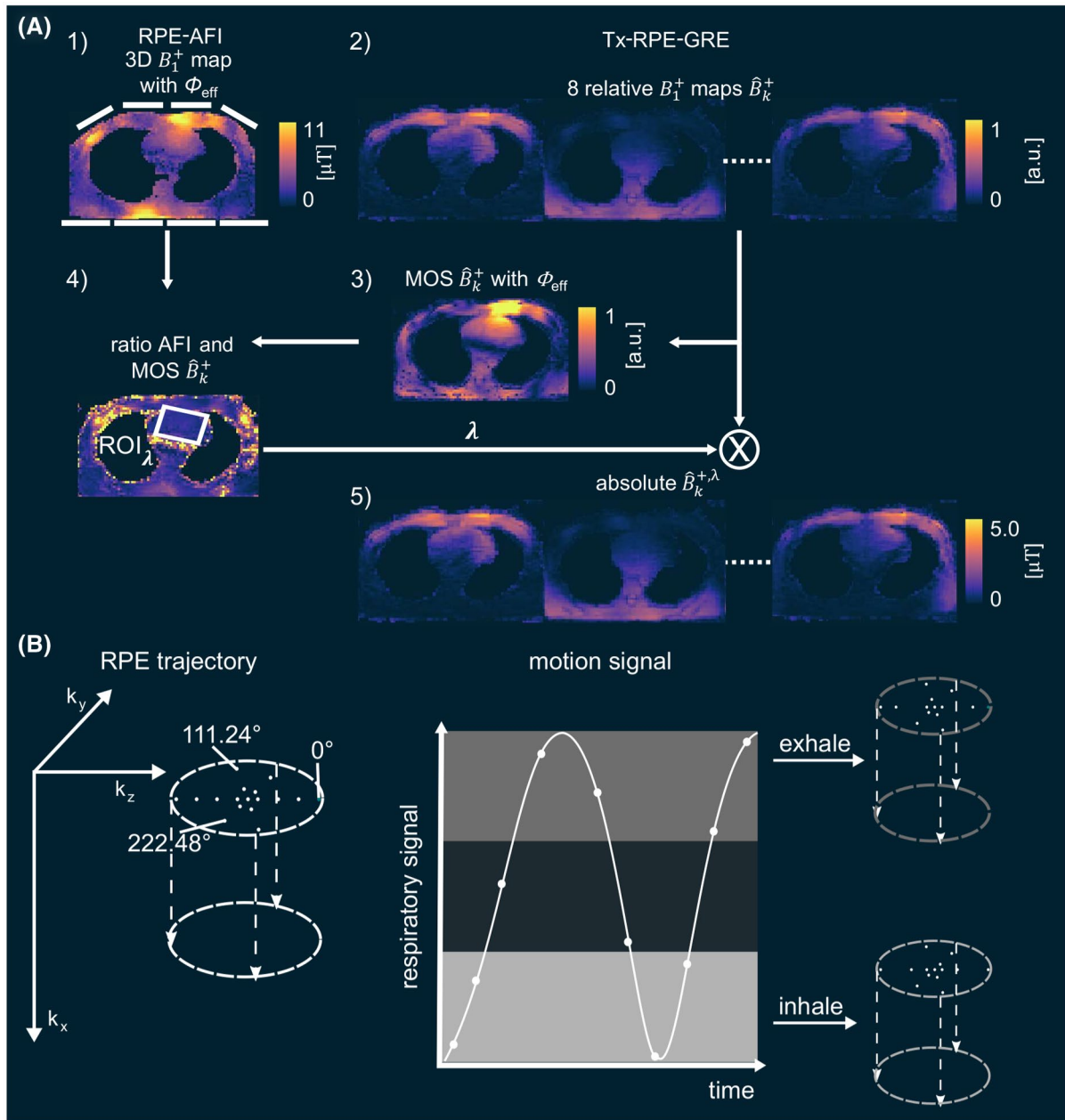
FIGURE 1 A, Workflow of proposed B_1^+ mapping approach that uses acquired AFI data (with white lines as coil locations) (1) and calculated magnitude of the sum (MOS) of estimated channel-wise B_1^+ for efficient shim setting (2,3) to calculate calibration factor λ (4) resulting in channel-wise estimated, absolute B_1^+ maps (5). RPE trajectory with Cartesian data acquisition along readout direction k_x on a radial grid in the phase-encoding plane $k_y - k_z$. Between successive radial lines, the angle is increased by the golden angle, k-space data are retrospectively binned into different respiratory motion states with the help of a motion surrogate. B, Each bin is reconstructed and RPE-GRE data for different respiratory motion states can be acquired. Data are taken from subject S4. RPE-AFI, radial phase-encoding-actual flip angle imaging; Tx-RPE-GRE, transmit-radial phase-encoding-gradient echo

in Figure 1B. k-Space is sampled on a Cartesian grid along the readout direction (k_x), whereas the two phase-encoding (PE) directions (k_y, k_z) are sampled on a non-Cartesian, radial grid. After completing the N_{PE} readouts along one radial line, the next radial line is rotated by a golden-angle increment of 111.24°. The resulting RPE trajectory covered the PE plane homogenously and allowed retrospective binning of the data into $p = (1, \ldots, N_p)$ respiratory motion states using self-navigation.

The N_p undersampled respiration-resolved k-space data sets are subsequently reconstructed using nonuniform fast Fourier transformation (NUFFT) based on an iterative sensitivity-encoding (SENSE) algorithm.[23,26,27] A respiratory motion surrogate for self-navigation is retrieved from the 1D projection in the head–feet direction for $k_y = k_z = 0$.[23] The temporal sampling intervals for self-navigation and the number of readouts per radial line are listed in Table 1 for the different acquisitions.

2.2 | 3D Multichannel Tx-RPE-GRE and reconstruction of relative B_1^+ map

In the Tx-RPE-GRE acquisition, the RPE scheme is applied to a small tip angle GRE sequence, which consisted of $N_{Tx} + 2$ repetitive RPE-GRE scans. During each scan, only a single Tx channel is active while the signal is received through all $m = (1, \ldots, N_{Rx})$ Rx elements.[14,28] The active Tx channel number $k = (1, \ldots, N_{Tx})$ was incremented through the scans. In addition to the N_{Tx} scans, we acquired another scan with all N_{Tx} channels and one with no Tx channel active for transmission. The latter scan is used for noise decorrelation of the receive channels used during image reconstruction.

The magnitude of the resulting 3D respiration-resolved image $|I_{k,m,p}(\boldsymbol{r})|$ of Tx channel k, Rx channel m, and respiratory phase p for each spatial position $\boldsymbol{r}$ was then given by the simplified signal equation:

$$\left| I_{k,m,p}(\boldsymbol{r}) \right| = c \left| B_{m,p}^-(\boldsymbol{r}) \right| \cdot \left| B_{k,p}^+(\boldsymbol{r}) \right| \rho_0(\boldsymbol{r}), \quad (1)$$

with the complex receive profile $B_{m,p}^-(\boldsymbol{r})$, the complex transmission profile $B_{k,p}^+(\boldsymbol{r})$, the proton density $\rho_0(\boldsymbol{r})$, and the spatially independent, complex scaling factor c including RF pulse, hardware, and reconstruction-related scaling factors. Consequently, the sum of all magnitude images $\sum_{m}^{N_{Rx}} \sum_{k}^{N_{Tx}} |I_{k,m,p}(\boldsymbol{r})|$ can be computed across Tx and Rx

TABLE 1 Sequence parameter of in vivo and phantom studies with TR, TE, TA, oversampling as a percentage of phase-encoding points additionally acquired compared with a fully sampled Cartesian scan with the same FOV and voxel size, FA, BW, and self-navigation TS of k-space center

In vivo	RPE–AFI	Tx-RPE–GRE	RPE–GRE	Tx-GRE
TR1 [TR2] (ms)	10 [50]	5	3.7	5.2
TE (ms)	2.02	2.02	1.75	2.87
TA (min)	6.10	3.40	5.55	0.25
Oversampling	—	—	2.91	—
Nominal FA (degree)	90	20	25	15
Reference voltage (V)	170			
FOV (mm³)	250×312–350×312–350			$384 \times 384 \times 4$
Voxel size (mm³)	$4 \times 4 \times 4$	$4 \times 4 \times 4$	$1.4 \times 1.4 \times 1.4$	$4 \times 4 \times 4$
BW (kHz)	25.54	25.54	172.48	48.96
Self-navigation TS (ms)	480	80	162	—
Radial lines	384	256	2048	
Slices				3
Slice gap (mm)				20
Phantom	**RPE–AFI**	**Tx-RPE–GRE**		
TR1 [TR2] (ms)	10 [50]	4.26		
TE (ms)	1.9	1.9		
TA (min)	6.10	4.36		
Oversampling	—	0.5		
Nominal FA (degree)	60	5		
Reference voltage (V)	30	30		
FOV (mm³)	$200 \times 150 \times 150$	$200 \times 150 \times 150$		
Voxel size (mm³)	$3.1 \times 3.1 \times 3.1$	$3.1 \times 3.1 \times 3.1$		
BW (kHz)	25.54	25.54		
Self-navigation TS (ms)	480	140		
Radial lines	384	192		

AFI, actual flip angle imaging; BW, readout bandwidth; FA, flip angle; FOV, field of view; GRE, gradient echo; RPE, radial phase-encoding; TA, acquisition time; TE, echo time; TR, repetition time; TS, sampling time; Tx, transmit.

channels. Assuming that the sum of magnitudes (SOM) of all Tx channels is equal to the SOM of all Rx channels, which has been observed to fit well for transceiver coils,[14] then:

$$\sum_k^{N_{Tx}} \left| \widehat{B}_{k,p}^+(\boldsymbol{r}) \right| = \sqrt{\left(\frac{\sum_m^{N_{Rx}} \sum_k^{N_{Tx}} |I_{k,m,p}(\boldsymbol{r})|}{c\rho_0(\boldsymbol{r})} \right)} \quad (2)$$

This assumption introduced a bias into the resulting B_1^+ maps that is proportional to the square root of the proton density and symbolized by the hat. Estimated, relative $\widehat{B}_1^+$ magnitude maps were obtained for each Tx channel k and respiratory motion state p by weighting the expression (Equation 2) by relative image signal intensities $R_{k,p} = \left| \sum_m^{N_{Rx}} I_{k,m,p}(\boldsymbol{r}) \right| / \left. \sum_m^{N_{Rx}} \sum_k^{N_{Tx}} \right| I_{k,m,p}(\boldsymbol{r}) \Big|^{[14]}$:

$$\left| \widehat{B}_{k,p}^+(\boldsymbol{r}) \right| = R_{k,p}(\boldsymbol{r}) \cdot \sum_k^{N_{Tx}} \left| \widehat{B}_{k,p}^+(\boldsymbol{r}) \right| = \frac{\left| \sum_m^{N_{Rx}} I_{k,m,p}(\boldsymbol{r}) \right|}{\sqrt{c\rho_0(\boldsymbol{r}) \sum_m^{N_{Rx}} \sum_k^{N_{Tx}} |I_{k,m,p}(\boldsymbol{r})|}}$$

$$(3)$$

Relative Tx phase maps $\phi_{k,p}(\boldsymbol{r})$ of Tx channel k relative to one fixed Tx channel k_f are calculated based on the complex images by:

$$\phi_{k,p}(\boldsymbol{r}) = \arg \left[\sum_m^{N_{Rx}} I_{k,m,p}(\boldsymbol{r}) I_{k_f,m,p}^*(\boldsymbol{r}) \right].$$

Here, $*$ denotes the complex conjugate and arg is the phase of the complex value. The resulting estimated B_1^+ maps were finally given by:

$$\widehat{B}_{k,p}^+(\boldsymbol{r}) = \left| \widehat{B}_{k,p}^+(\boldsymbol{r}) \right| \cdot e^{i\phi_{k,p}(\boldsymbol{r})}. \quad (4)$$

Two different sets of $\widehat{B}_{k,p}^+(\boldsymbol{r})$ maps are derived. A set of nonrespiration-resolved B_1^+ maps $\widehat{B}_k^+(\boldsymbol{r})$ with $N_p = 1$ is reconstructed during the actual imaging session using all acquired data without any binning. A second set of respiration-resolved B_1^+ estimations $\widehat{B}_{k,p}^+(\boldsymbol{r})$ with $N_p = 3$ is obtained retrospectively after each session because of reconstruction time limitations.

The nonrespiration-resolved $\widehat{B}_k^+(\boldsymbol{r})$ maps obtained with the default transmission phase ϕ_0 are used to compute two static phase-only B_1^+ shim settings based on multiple manually drawn ROIs covering multiple slices. The first shim setting is computed for three transversal-slice ROIs covering the human heart, by following the heart–lung border, to obtain a homogenous B_1^+ shim ϕ_{hom}. The central slice S_c is placed in the center of the heart, along the head–feet direction; the other two slices are placed above and below S_c. The second

shim setting is computed for a ROI_{eff} with a diameter of 2 to 3 cm, in a single transversal slice to obtain an RF-efficient B_1^+ shim ϕ_{eff} in an ROI covering the anterior section of the heart and myocardium. The efficiency is computed as in Metzger et al[4] and aimed to maximize the constructive interference of the $N_{Tx}B_1^+$ maps in the target region.

The phase setting ϕ_{hom} is applied to achieve homogeneous FAs in subsequently acquired high-resolution 3D RPE-GRE acquisitions, as well as 2D Cartesian cine GRE scans; ϕ_{eff} is applied for an RPE-AFI mapping as outlined below.

2.3 | 3D RPE-AFI

An RPE-GRE acquisition scheme was modified to acquire two interleaved repetition times (TRs; RPE-AFI),[24] which enables the computation of absolute, respiration-resolved B_1^+ maps according to the AFI approach.[11] The RPE-AFI data is acquired in vivo with B_1^+ shim setting ϕ_{ef}. Each readout of the RPE k-space trajectory is consecutively sampled twice with different TR (ratio $n = TR_2 / TR_1$) in an interleaved fashion, which results in N_p respiration-resolved image data sets $A_{1,p}(\boldsymbol{r})$ and $A_{2,p}(\boldsymbol{r})$. The FA $\alpha_p(\boldsymbol{r})$ for each motion state p and spatial position $\boldsymbol{r}$ is computed following Yarnykh.[11]

Before the FA calculation, $A_{1,p}(\boldsymbol{r})$ and $A_{2,p}(\boldsymbol{r})$ is median filtered within a three-voxel neighborhood. The obtained FA $\alpha_p(\boldsymbol{r})$ in degree is converted to absolute B_1^+ maps, termed $B_p^{+AFI}(\boldsymbol{r})$, which are given in μT or related to unit power in $μT/\sqrt{kW}$.

2.4 | Reconstruction of unbiased and estimated, absolute multichannel $\mathbf{B}_1^+$ maps

Unbiased, respiration-resolved, absolute B_1^+ maps of each Tx channel are obtained following Van de Moortele et al,[12] and by combining the RPE-AFI with the images obtained by the Tx-RPE-GRE acquisition. This approach, however, requires a sufficiently high FA of $>20°$ throughout the body, which is not achievable in the center of the body with our set-up because of RF power limitations.

To circumvent this, a different approach is used as already suggested in Van de Moortele et al[14] for brain applications by calculating a single scaling factor λ based on the RPE-AFI acquisition in a manually drawn ROI_λ with a sufficiently high FA of $>40°$ (as shown in Figure 1A).

$$\lambda = \left. \frac{B_p^{+AFI}}{\left| \sum_k^{N_{Tx}} \widehat{B}_{k,p}^+(\boldsymbol{r}) e^{i\phi_{eff}} \right|} \right|_{ROI_\lambda}. \quad (5)$$

To achieve this calibration, the same efficient B_1^+ shim ϕ_{eff} is retrospectively applied to the $\widehat{B}_{k,p}^+(r)$ maps. The scaling factor λ is subsequently applied to the relative $\widehat{B}_{k,p}^+(r)$ maps (Equation 4) to yield estimated, absolute B_1^+ maps, termed $\widehat{B}_{k,p}^{+,\lambda}(r)$ in the following:

$$\widehat{B}_{k,p}^{+,\lambda}(r) = \lambda\,\widehat{B}_{k,p}^+(r). \tag{6}$$

2.5 | Experiments

All scans were obtained on a 7T system (Magnetom 7T; Siemens Healthcare, Erlangen, Germany) equipped with a pTx system and 8×1 kW amplifiers (Stolberg AG, Stolberg, Germany). The phantom study was performed using an in-house-built 8 Tx/8 Rx transceiver head coil. The in vivo measurements were performed with a commercial body coil array (MRI Tools, Berlin, Germany), consisting of 32 transceiver elements (eight dipoles and 24 loops) that are driven in an 8 Tx/32 Rx channel mode. The body coil has a field-of-view (FOV)/excitation of approximately 240 mm along the head–feet direction. It consists of an anterior and a posterior half with fixed, solid housings. The anterior and posterior halves have four parallel aligned blocks with four elements each: one dipole and three loop elements. The three loop elements are distributed along the head–feet direction and each loop element covers approximately one-third of the dipole. In the Tx case, the blocks of one dipole and three loop elements are combined with fixed phases to form one Tx channel, respectively. The body coil was certified by a notified body to comply with the local specific absorption rate (SAR) limits in a first-level controlled mode of 20 W/kg (IEC 60601-2-33) that were ensured by limiting the RF power for each Tx channel to the body coil. The conversion from RF power to a local SAR was estimated based on electromagnetic simulations with 10 million random-phase settings. The worst-case shim combined with an RF power of 11.8 W applied to each Tx channel resulted in a 10 g-averaged peak spatial SAR of 11.1 W/kg; thus, it left an additional safety margin factor of 1.8. Although such limits are then independent of the applied Tx phase setting, the approach provides rather conservative power limits.

To validate the respiration-resolved B_1^+ maps, a cylindrical motion phantom (radius = 12.5 cm, height = 12.0 cm) filled with water, 2% agaroses, 0.2% sodium chloride, 0.1% copper sulfate (which corresponds to $\sigma_{phantom}$ = 0.4 s / m, ε_r = 80) was used that performed a translational sinusoidal-like motion along the bore axis with a peak-to-peak amplitude of 3 cm and a frequency of 0.1 Hz. To perform this motion, the phantom was placed on a wagon driven by a piston that was attached to a flywheel. The rotation of the flywheel was controlled by a

cord that was wound on the flywheel. This cord was unwound by a step motor located in the operator room. Tx-RPE-GRE and RPE-AFI data sets were acquired during the translational movement of the phantom, referred to as "dynamic" acquisition. For comparison, RPE-AFI and Tx-RPE-GRE data were acquired for two extreme motion states of the phantom mimicking an inhale and exhale state, referred to as "static" acquisition. Sequence parameters are listed in Table 1. RPE-AFI and Tx-RPE-GRE data were low-pass-filtered before NUFFT reconstruction. For binning, self-navigation was used to reconstruct data into three different respiratory motion states using an iterative SENSE algorithm.[23,26,27]

2.6 | In vivo acquisitions

Eleven healthy subjects (age: 30 ± 5 years, max/min: 35/21 years; body mass index [BMI]: 24 ± 5 kg/m^2, max/min: 34/19 kg/m^2; male/female: 8/3) were included in this study after obtaining ethical approval of the study by PTB's local institutional review board and after the subjects provided written informed consent.

All subjects underwent the same protocol, which started with the coil's default B_1^+ shim and no additional Tx phase. The default shim is set by the manufacturer as a trade-off between B_1^+ power efficiency, SAR efficiency, and avoidance of voids throughout the entire ascending aorta, descending aorta, and the heart. This default shim is used only as a starting point because the maps and the resulting excitation pattern vary within subjects. In this configuration, a Tx-RPE-GRE was acquired under free-breathing; for comparison, a Cartesian multichannel GRE sequence (2D-Tx-GRE) was applied to obtain three equidistant transversal 2D slices without cardiac gating within one breath-hold. Additionally, a high-resolution RPE-based anatomical GRE acquisition (RPE-GRE) was obtained with default B_1^+ shim. After calculation of ϕ_{eff} based on the $\widehat{B}_{k,p}^+(r)$ maps generated by Tx-RPE-GRE reconstructed with $N_p = 1$ and Equation 4, an RPE-AFI was obtained with phase setting ϕ_{eff}. Here, $TR_1 = 10$ ms, $TR_2 = 50$ ms was used, thus at the lower end within the range recommended by Yarnykh,[11] which reduced acquisition time and allowed a k-space center update of 0.48 seconds needed for sampling the self-navigation signal. Additionally, B_1^+ mapping was performed under a deep-breathing condition in two healthy subjects (S10 and S11). In these two cases, the data were reconstructed into $N_p = 5$ respiratory motion states, which required doubling the acquisition time of both RPE-AFI and Tx-RPE-GRE with otherwise same acquisition parameters. Thus, $p = 5$ indicates the end inspiration motion state for deep breathing; $p = 3$ indicates the end inspiration motion state for shallow breathing. All RPE acquisitions were carried out with a rectangular pulse with a pulse duration of 0.5 ms.

To demonstrate the shimming results, an additional 3D RPE-GRE sequence, with 1.4 mm isotropic resolution was acquired under free-breathing without cardiac triggering or gating, and 2D cine GRE acquisitions in transverse orientation were performed with a homogenous B_1^+ shim setting ϕ_{hom}, with acquisition parameters listed in Table 1. In one subject (S8), additional 2D cine GRE scans were acquired during breath-holds in four-chamber, long-axis and short-axis views with a TR = 4.4 ms, echo time = 2.0 ms, acquisition time = 17 s, FOV = $384 \times 272 \times 5$ mm^3, voxel-size = $1.3 \times 1.3 \times 5$ mm^3, nominal FA = 50°, generalized autocalibrating partially parallel acquisitions (GRAPPA) factor = 2 with 24 reference lines, retrospective electrocardiogram (ECG) gating, and 30-ms reconstructed temporal resolution yielding 46 cardiac phases.

2.7 | Image reconstruction

The Tx-RPE-GRE–based data were reconstructed during the in vivo data acquisition on a separate computer (12 central processing units (CPUs) with 2.1 GHz and 128 GB of random-access memory (RAM)). To reconstruct nonrespiration-resolved RPE-GRE data, which have been used to calculate the $\widehat{B}_k^+ (\boldsymbol{r})$ maps used online during the same scanning session, a NUFFT was applied.[26] The respiration-resolved data sets were reconstructed after the scanning session on a separate reconstruction computer with 24 CPUs and 256 GB RAM. Undersampled RPE data was reconstructed for $N_p = 3$ respiration-resolved states using a NUFFT iterative SENSE reconstruction.[27] Respiratory binning was performed using a self-navigation approach[23] and a sliding window with a 20% overlap for each side of the bin. The 3D RPE-GRE sequence obtained for the shimming demonstration was reconstructed using iterative SENSE reconstruction, resulting in 3D images in four different respiratory motion states. Subsequently, a single set of high-resolution, respiratory motion-corrected RPE-GRE images I$_{MOCO}$ was obtained based on the motion fields from the four states. To this end, nonrigid motion fields were estimated using NIFTYREG[29] according to an algorithm outlined in Cruz et al[21] and Kolbitsch et al.[30]

2.8 | Data analysis

Quantitative evaluation was performed for an ROI computing the mean efficiency and the coefficient of variation (CV) following Metzger et al[4] and Schmitter et al.[28] The mean efficiency was defined as

$$\eta = \text{mean} \left(\frac{\left| \sum_k^{N_{Tx}} \widehat{B}_{k,p}^{+,\lambda} (\boldsymbol{r}) e^{i\phi_k} \right|}{\sum_k^{N_{Tx}} \left| \widehat{B}_{k,p}^{+,\lambda} (\boldsymbol{r}) \right|} \right) \Bigg|_{ROI},$$

with $\left| \sum_k^{N_{Tx}} \widehat{B}_{k,p}^{+,\lambda} (\boldsymbol{r}) e^{i\phi_k} \right|$ being the magnitude of the sum (MOS) and $\sum_k^{N_{Tx}} \left| \widehat{B}_{k,p}^{+,\lambda} (\boldsymbol{r}) \right|$ being the SOM of a channel-wise Tx field $\widehat{B}_{k,p}^+ (\boldsymbol{r})$ for a phase settings ϕ_k.[31] The CV was defined as

$$CV = \frac{SD \left(\left| \sum_k^{N_{Tx}} \widehat{B}_{k,p}^{+,\lambda} (\boldsymbol{r}) e^{i\phi_k} \right| \right)}{\text{mean} \left(\left| \sum_k^{N_{Tx}} \widehat{B}_{k,p}^{+,\lambda} (\boldsymbol{r}) e^{i\phi_k} \right| \right)} \Bigg|_{ROI},$$

with standard deviation SD. Moreover, pixel-wise differences between B_1^+ estimations were computed to quantify the accuracy of the proposed B_1^+ mapping approach. The difference between static and dynamic phantom experiments was analyzed based on the MOS of static and dynamic $\widehat{B}_k^{+,\lambda} (\boldsymbol{r})$ maps in a Bland-Altman plot along with ± 1.96 SD and mean values over the whole volume. Nonrespiration-resolved and respiration-resolved mean $\widehat{B}_{k,p}^{+,\lambda}$ distributions were analyzed in line plots, showing a mean value of three slices. The magnitude and phase differences between 2D $\widehat{B}_k^{+,\lambda} (\boldsymbol{r})$ maps and 3D $\widehat{B}_k^{+,\lambda} (\boldsymbol{r})$ maps were analyzed in line plots for a matched slice and manually selected lines.

All results were masked based on thresholded low-pass filtered magnitude images with a kernel size of five voxels. For Tx-RPE-GRE, the SOM of Tx channels was used.

3 | RESULTS

In this section we show the acquisition and reconstruction of respiration-resolved 3D absolute B_1^+ estimations of a moving phantom and the human thorax at 7T for 11 subjects with a wide range of BMIs and body dimensions. The figures illustrate the changes compared with previous techniques applied in the body: the extension from 2D to 3D, the ability to provide respiration-resolved maps, and the change from relative to absolute maps. The validity of the B_1^+ maps is shown by a static phase-only B_1^+ shim and successive cine GRE acquisitions.

Figure 2 depicts motion-resolved $\widehat{B}_{k,p}^{+,\lambda}$ maps, each obtained from threefold undersampled k-space data in the motion phantom experiments from the dynamic scan in comparison with the static reference obtained from fully sampled data. Depicted are the magnitude and phase images of two motion states (mimicking inhale and exhale) for qualitative comparison and a Bland-Altman plot of the difference between the static and dynamic MOS of $\widehat{B}_{k,p}^{+,\lambda}$ maps for inhale and exhale, respectively. Bland-Altman plots show the voxel-wise difference for the whole phantom between the MOS of the dynamic $\widehat{B}_{k,p}^{+,\lambda} (\boldsymbol{r})$ and static $\widehat{B}_k^{+,\lambda} (\boldsymbol{r})$ measurement with absolute (relative) mean difference $B_1^+ = 1.2 \pm 2.6$ μT/$\sqrt{kW}$
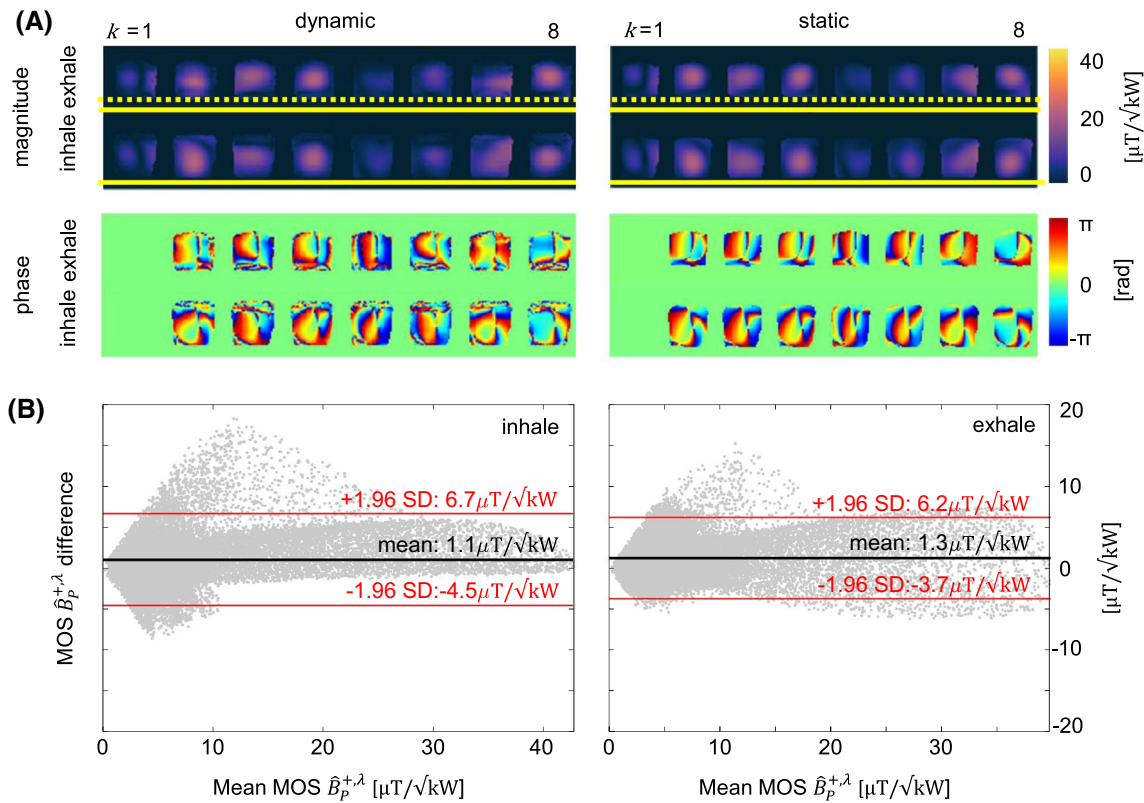
FIGURE 2 A, Comparison of magnitude and phase of estimated, absolute B_1^+ maps with dynamic data with exhale and inhale motion states, and data from static acquisition for exhale and inhale position, with inhale position indicated by a solid line and exhale position by a dashed line, with a peak-to-peak difference of 30 mm. All transmit channels of the dynamic scan show qualitatively comparable results in terms of magnitude and phase distribution compared with the static reference images. B, Bland-Altman plot from MOS of B_1^+ maps with voxel-wise difference of static to dynamic acquisition as a function of voxel-wise estimated mean B_1^+ map is shown for inhale and exhale position of the phantom. With a mean difference of $B_1^+ = 1.1 \pm 2.9\ \mu T/\sqrt{kW}$ for inhale position and mean difference $B_1^+ = 1.3 \pm 2.6\ \mu T/\sqrt{kW}$ for exhale position. MOS, magnitude of the sum

(3% $\pm$ 6%) in the exhale position and a mean difference $B_1^+ = 1.2 \pm 2.9\ \mu T/\sqrt{kW}$ (3 $\pm$ 6%) in the inhale position. Background voxels were excluded from the analysis.

Figure 3 illustrates the measured $\widehat{B}_{k,p}^{+,\lambda}$ of subject S4 in transversal and sagittal view for Tx channel $k = 1, 3$ (Figure 3A,B). Differences in $\widehat{B}_{k,p}^{+,\lambda}$ between exhale and inhale of up to 15% and between nonrespiration-resolved and exhale/inhale of up to 10% and 7%, respectively, have been found.

Figure 4A shows channel-wise 2D Cartesian and 3D non-respiration-resolved RPE $\widehat{B}_{k,p}^{+,\lambda}$ maps for each Tx channel in a transversal view of the isocenter in subject S8. All 3D $\widehat{B}_{k,p}^{+,\lambda}$ maps show comparable results in terms of magnitude and phase distribution compared with the 2D reference images; none of the channels shows motion artifacts. Consistent results were found for all subjects. Quantitative comparison was carried out with line plots for cross sections through the heart of the central slice for Tx channel $k = 2, 4$ (Figure 4B,C) for phase and magnitude of 2D Cartesian (red) and 3D RPE-based $\widehat{B}_{k,p}^{+,\lambda}$ (black).

Figure 5 illustrates the 3D absolute $B_p^{+,AFI}$ maps (RPE-AFI) acquired with shim setting Φ_{eff} and absolute $\widehat{B}_k^{+,\lambda}$ maps acquired

with shim setting Φ_0 that have been combined retrospectively with shim setting Φ_{eff}. There is an excellent match between both maps in the heart region, thus demonstrating the validity of combining relative and absolute maps and to calculate the calibration factor λ used to compute the absolute $\widehat{B}_k^{+,\lambda}$ maps.

The resulting CV and efficiency η for all volunteers are shown in Figure 6, with values calculated in a region covering three transversal slices of the heart as can be seen in Figure 7. Across all subjects, the variations in the ROI could be substantially reduced from $CV_{pre} = 42.5\% \pm 6.2\%$ to $CV_{post} = 20.6\% \pm 2.0\%$ for Φ_{hom}. The mean efficiency was improved from $\eta_{pre} = 53.2\% \pm 11.2\%$ to $\eta_{post} = 90.0\% \pm 7.5\%$ for Φ_{eff}.

Figure 7 depicts a qualitative comparison of $\widehat{B}_k^{+,\lambda}$ maps and RPE-GRE images obtained for two different shim settings for one coronal and three transversal views. Figure 7A shows the results using the default phase setting Φ_0, resulting in signal cancellations in the human heart. Importantly, the B_1^+ maps qualitatively match the experimental RPE-GRE images and predict the underlying B_1^+ artifacts denoted by the yellow arrows. Figure 7B shows the results after the homogeneous B_1^+ shim setting Φ_{hom}. The CV in these acquisitions
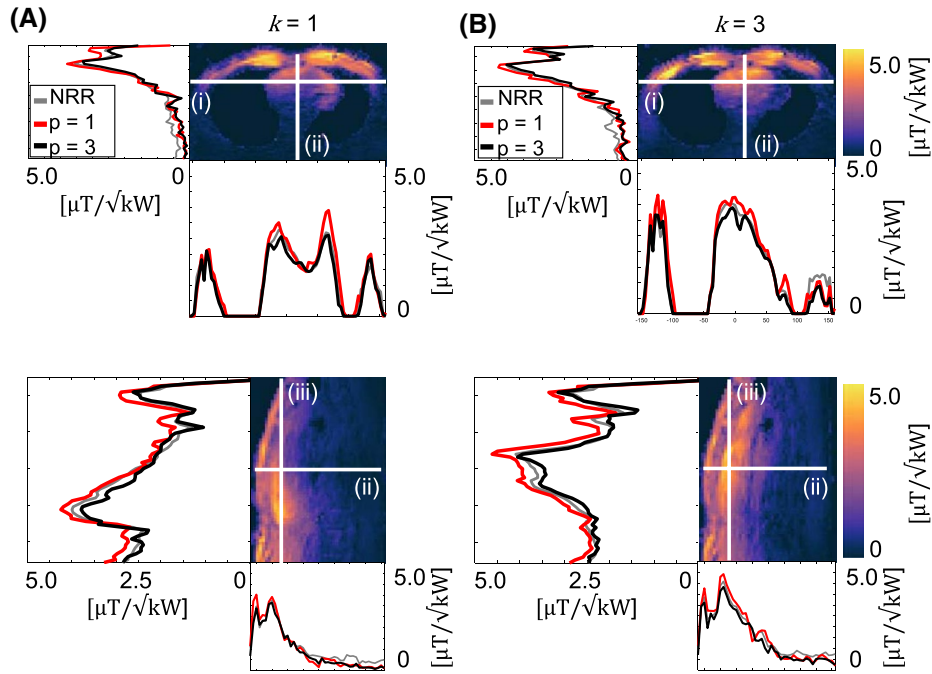
FIGURE 3 Comparison of magnitude distribution between nonrespiration-resolved (NRR) exhale ($P = 1$) and inhale ($P = 3$) motion states for transmit channel $k = 1$ (A) and $k = 3$ (B) in transversal and sagittal view for subject S4. Positions of one-dimensional B_1^+ curves for NRR exhale ($P = 1$) and inhale ($P = 3$) motion states are indicated by solid white lines for left–right (i), anterior–posterior (ii), and head–feet (iii) direction

was reduced from 42.9% (Φ_0) to 19.8% (Φ_{hom}), which is reflected by the improved homogeneity.

In Figure 8, respiration-resolved 3D RPE-GRE images in comparison with the MOS of respiration-resolved 3D $\widehat{B}_p^{+,\lambda}$ maps are featured. The mean free-breathing difference of the position of the right hemidiaphragm between inhales and exhales was 12.1 ± 2.6 mm. Cross sections of the B_1^+ distribution through the heart in coronal view (indicated by the solid white line) for exhale and inhale show $\widehat{B}_p^{+,\lambda}$, a (relative) difference up to 0.21 μT (24%), with mean $\widehat{B}_p^{+,\lambda}$ of 0.74 μT, between both respiratory motion states. The respiration-resolved $\widehat{B}_p^{+,\lambda}$ maps are free from motion artifacts and match the experimental data.

$\widehat{B}_k^{+,\lambda}$ magnitude and phase distribution for Tx channel 1 are illustrated in three different respiratory motion states p for exhale, inhale, and the nonrespiration-resolved reconstruction for subject S10 performing deep breathing in Figure 9. No motion artifacts are visible in the respiration-resolved images, and a clear difference between the $\widehat{B}_k^{+,\lambda}$ distributions for the exhale and inhale motion state is visible. The spatial displacement of the right hemidiaphragm between inhale and exhale was approximately 30 mm.

4 | DISCUSSION

The presented respiration-resolved, absolute multichannel B_1^+ mapping method is based on a relative B_1^+ mapping method,[14] providing proton-density relative 2D B_1^+ maps in the human head. That technique has also been applied to the human body at UHF to derive relative 2D B_1^+ maps within a single slice or multiple slices to calculate B_1^+ shimming solutions. Furthermore, it has been applied to optimize the B_1^+ field at 7T within various organs in the human body including the aorta and the kidney, as well as the human heart.[15,16,32] In addition, such a method has been used to calculate and apply multispoke pulses in the human heart and the liver at 7T,[5,33,34] as well as at 10.5T.[18] The present method extends this aforementioned technique with three modifications: (1) by extending it to 3D mapping in the human body, (2) by providing respiration-resolved maps, and (3) by enhancing the 3D AFI technique to allow for generating respiration-resolved absolute B_1^+ maps in the human body. The latter is used for calibration of the channel-wise maps. 3D mapping of the Tx field is highly beneficial when B_1^+ shim solutions or pTx pulses are calculated for an entire 3D volume of interest. The resulting maps provide the flexibility to either optimize the B_1^+ field for a single slice or multiple slices in (multislice) 2D imaging or for the entire volume in 3D imaging.[1]

The ability to obtain B_1^+ maps with calibrated magnitude is important for many applications, as it allows us to adjust the absolute FA value. In this work, relative maps obtained from the Tx-RPE-GRE acquisition were combined with an RPE-AFI acquisition that provides respiration-resolved B_1^+ maps. Because this method uses GRE acquisitions obtained in the linear, small FA regime to calculate the relative B_1^+ maps, the technique does not require high power levels.
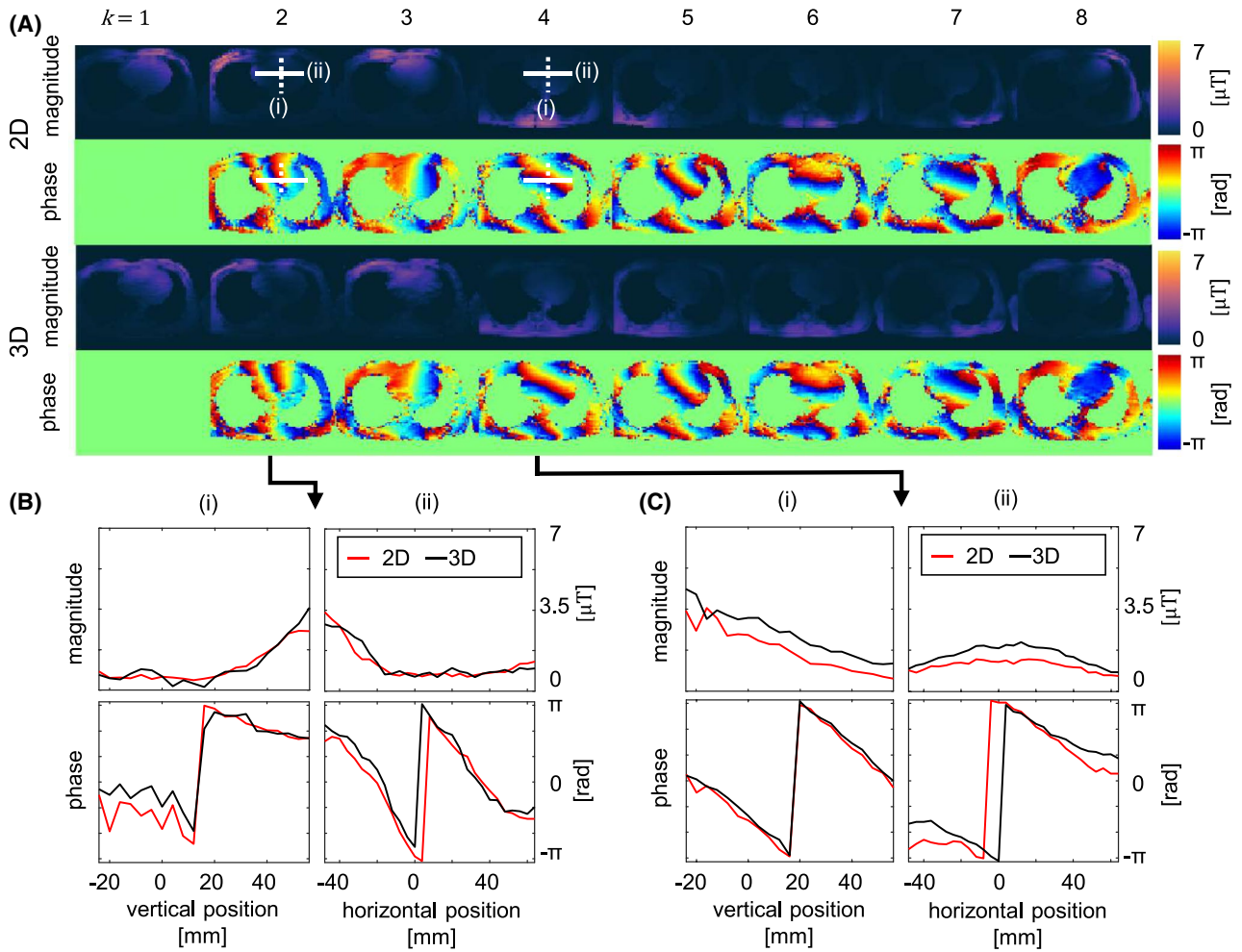
FIGURE 4 A, Magnitude and phase from two-dimensional (2D) and three-dimensional (3D) estimated, absolute B_1^+ maps for each transmit channel k for isocenter of subject S8. Vertical (dotted) and horizontal (solid) profiles of phase and magnitude for 2D B_1^+ estimation (red) and 3D B_1^+ estimation (black) of transmit channel k = 2 (B) and k = 4 (C). The solid and dashed line in phase images indicates the position of line plot data
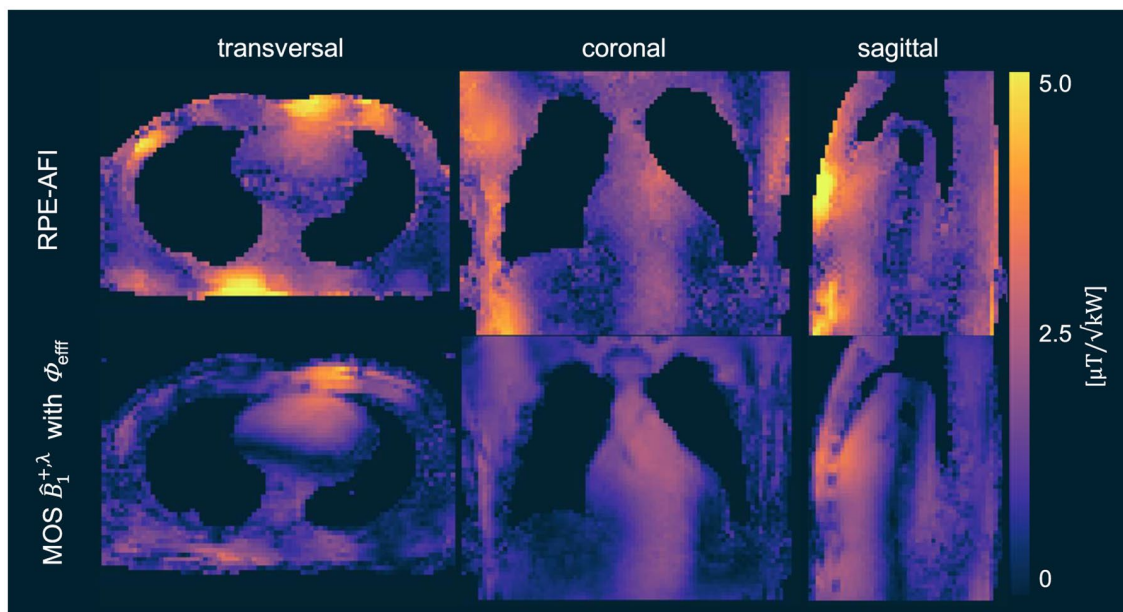
FIGURE 5 In vivo RPE-AFI maps $B_1^{+,AFI}$ measured with Φ_{eff} of the human body with an estimation of B_1^+ shim setting Φ_{eff} from MOS of estimated, absolute B_1^+ for subject S4. Images correspond to three cross sections taken from a three-dimensional volume. MOS, magnitude of the sum; RPE-AFI, radial phase-encoding-actual flip angle imaging
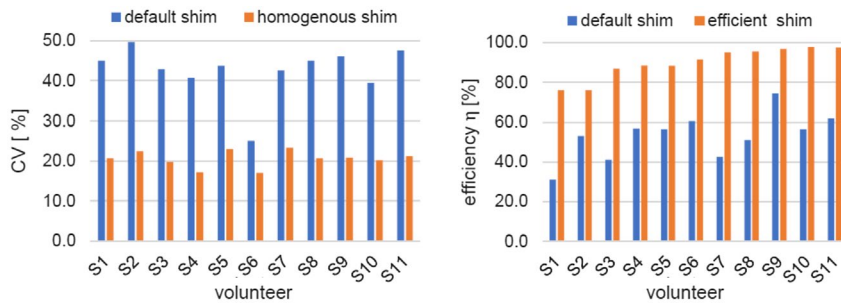
FIGURE 6 Calculated values of the coefficient of variation (CV) and the efficiency η of the B_1^+ shim settings evaluated in hand-drawn regions of interest around the hearts of all 11 subjects
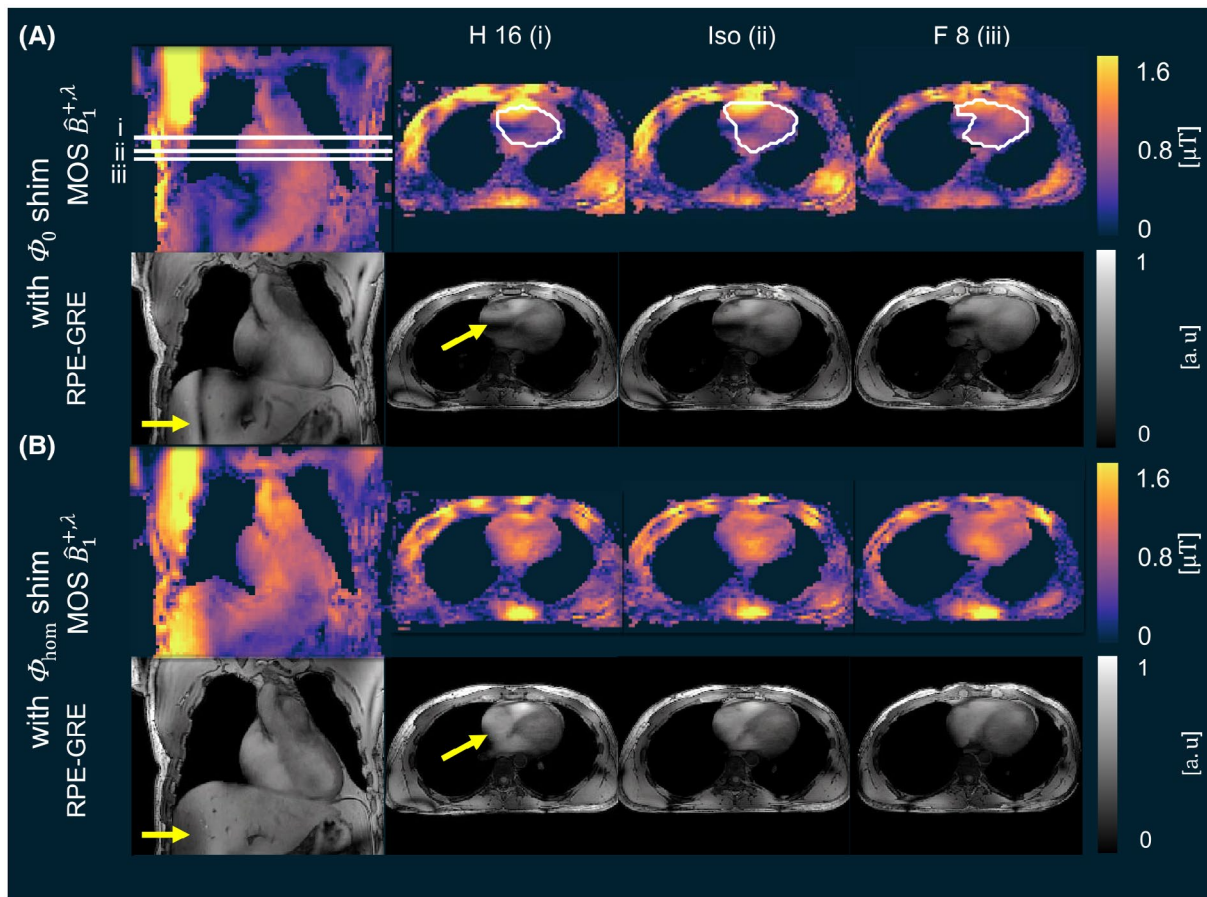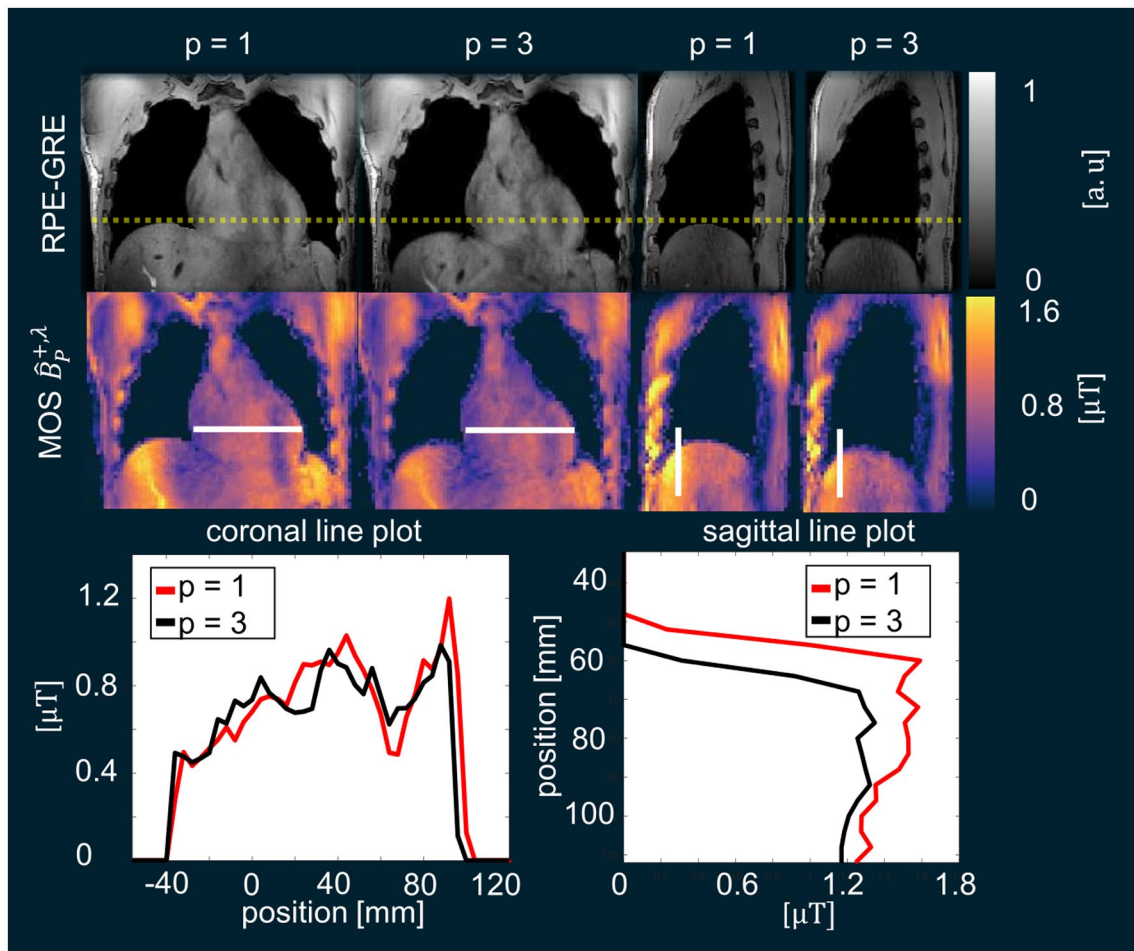

FIGURE 7 A, Estimated, absolute B_1^+ distribution for default shim setting Φ_0 in coronal view, with the positions of transversal slices indicated by white lines. The white circles mark the regions of interest (ROIs) for homogenous shim calculation as well as coefficient of variation (CV). Corresponding respiratory motion-compensated high-resolution RPE-GRE images I_{MOCO} are illustrated below for matching coronal and transversal slices obtained with Φ_0, with CV = 42.7% and η = 42.6%. B, Estimation of B_1^+ shim setting Φ_{hom} optimized for homogeneity in the ROI with CV = 19.5% and efficiency η = 51.7% for coronal and transversal view, as well as corresponding slices for I_{MOCO} obtained with Φ_{hom}. The yellow arrows denote the signal dropouts in (A) obtained with Φ_0 that are recovered in (B) by applying Φ_{hom}. Corresponding images are taken from subject S3. MOS, magnitude of the sum; RPE-GRE, radial phase-encoding-gradient echo

Nevertheless, the gradient of the individual B_1^+ profiles from the body surface towards the center of the body makes it challenging to stay within the linear regime close to the coil, while still providing sufficient SNR in the more distant body regions. On the one hand, we observed decreased SNR in the posterior part of the heart in some volunteers. On the other hand, T_1 effects may bias the resulting B_1^+ maps close to the skin, particularly when short TR values

are being used to keep the scan time short as is the case for cardiac B_1^+ mapping. This effect can be seen in the 3D map in Figure 4 that used a 25% higher FA compared with the 2D acquisition. Although the T_1 bias could be avoided by replacing the method with alternative techniques[35,36] that provide T_1 unbiased relative B_1^+ maps, such methods may increase the acquisition time multifold. Furthermore, a general challenge that is associated with the body size is

FIGURE 8 RPE–GRE image in two respiratory states (exhale/inhale) with the corresponding MOS of estimated, absolute B_1^+ distribution for subject S4 for B_1^+ shim setting Φ_{hom}. The yellow dashed line indicates the exhale position of the right hemidiaphragm. The solid white line denotes the position of line plot data. Images correspond to two cross sections taken from a three-dimensional volume. MOS, magnitude of the sum; RPE-GRE, radial phase-encoding-gradient echo

given by regions of low FA in which the AFI method does not yield reliable values. This problem could be avoided by acquiring two or more AFI maps with different shim settings so that at each point within the region at least one of the shim settings provides sufficient B_1^+. The latter option is also exploited by the TIAMO method.[37] In principle, a similar technique, as proposed in Van de Moortele et al[12] for the human brain, could be extended to the human body. In that approach, individual, absolute B_1^+ maps of each Tx channel are obtained by weighting relative Tx channel maps with one absolute B_1^+ map acquired by transmitting with all Tx channels combined with a given B_1^+ shim setting. This approach, however, was not feasible because it requires a well-defined FA map, ie, a FA > 20° throughout the entire 3D volume. In this work, a well-defined FA map could not be achieved in the center of the body given the power limits of the coil. We refrained from extending the duration of the rectangular RF pulse length because initial investigations showed altered FA values.

The AFI method could be replaced by other, less SAR demanding methods such as the DREAM technique,[9] which can provide very fast (ie, subsecond) absolute B_1^+ maps of the human body. Furthermore, the method has also been used to show respiration-induced B_1^+ changes in the human body at 3T.[38] However, the DREAM mapping technique is very sensitive to flow-induced artifacts,[39] which has also been confirmed by our own experiments, and it has a limited dynamic FA range.[9] Less flow/motion sensitivity has been observed by AFI. To estimate a potential FA error in the left ventricle and the myocardium (ie, within the ROI used for FA calibration), separate experiments in a flow phantom were conducted at 7T with a constant flow velocity of 55 cm/s, which corresponds to maximum intracardiac blood velocities[40] (see Supporting Information Figure S1). An average FA error of 15% was found compared with flow-off conditions. Furthermore, the impact of myocardial motion was estimated by extended phase graphs, which resulted in an estimated maximum error of <5%. The Bloch-Siegert shift mapping
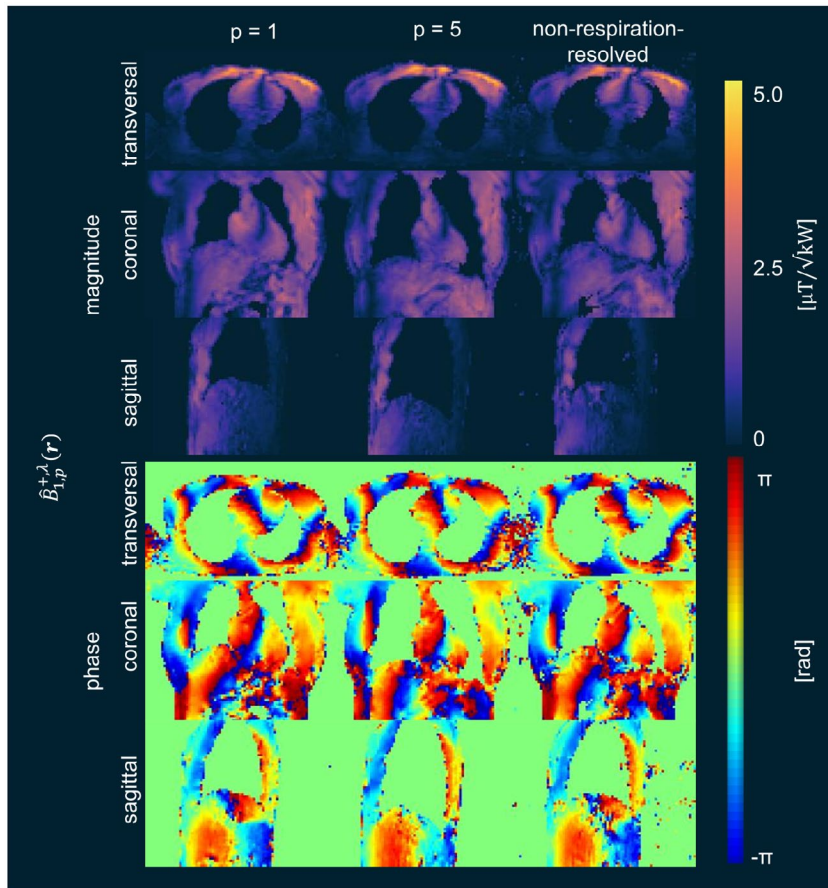
FIGURE 9 Estimated, absolute B_1^+ magnitude and phase distribution for transmit channel 1 in three different respiratory motion states: p for exhale ($P = 1$), inhale ($P = 5$), and the nonrespiration-resolved reconstruction for subject S10. No motion artifacts are visible in the respiration-resolved images, and a clear difference between the $\widehat{B}_k^{+,\lambda}$ distribution for exhale and inhale motion state is visible. The deep-breathing difference of the position of the right hemidiaphragm between inhale and exhale was approximately 30 mm

technique, however, could not be applied in the body at 7T because of SAR constraints.

Therefore, the approach of calibrating the relative respiration-resolved B_1^+ maps was employed in this work. Despite its benefits, the method has limitations. As reflected in Equation 2, the resulting maps are biased by the square-root of the proton density. The impact on the resulting B_1^+ maps, however, is expected to induce only minor tissue-dependent variations of a few percentages. Furthermore, the technique is biased by the assumption used to obtain Equation 2 (ie, the SOM of the receive signal equals the SOM of the Tx signal), which is particularly the case for the present coil, where groups of four coil elements were combined to a single Tx element. According to electromagnetic field simulations obtained with the Duke model[41] and performed for the applied 8 Tx/32 Rx body-coil configuration, this assumption introduces an error of 10% on average throughout the thorax. The error could be reduced to 5% if the RF coil could be driven with 32 Tx and 32 Rx channels, as shown in Supporting Information Figure S2. Nevertheless, despite those limitations, a high similarity was found in qualitative comparisons between the excitation patterns and the resulting images, which is in strong agreement with previous work where the same technique was applied slice selectively in 2D.[5,15]

The resulting absolute B_1^+ maps obtained by the proposed method enabled successful B_1^+ phase shimming as has been shown for cardiac imaging. The shim allowed for acquiring 2D cine GRE acquisitions (see Supporting Information Figure S3) in different views under breath-hold, as well as 3D respiration-resolved and respiration-corrected RPE-based GRE imaging of the entire thorax obtained under free-breathing, and in both cases, the image quality was substantially improved compared with the default shim. The magnitude of the absolute B_1^+ maps was used to calibrate the nominal FA for each sequence accordingly. In two subjects, we observed phase singularities in the B_1^+ maps of Tx channel 1, which was used as the reference channel. Based on calculating the phase difference, this effect translated into the B_1^+ maps of the other seven Tx channels. Although this effect could be avoided by changing the reference channel (see Supporting Information Figure S4), we did not observe any impact on the resulting B_1^+ phase shim magnitude; therefore, channel 1 was set as the reference Tx channel.

Our initial results found that a shim setting calculated on B_1^+ maps in a respiratory state p performs better than a shim calculated on nonrespiration-resolved B_1^+ maps for images acquired in motion state p. Furthermore, it seems that for shallow breathing patterns such differences in B_1^+ and CV are rather minor[42]; thus, a respiration-state–resolved reconstruction may not be needed. However, our initial results indicate that the effect becomes stronger when deep breathing

is performed, which is in agreement with a recent study.[43] However, more-detailed investigations are necessary to be able to provide a more comprehensive description of the underlying effects.

Both the scan time and the reconstruction time are limitations of this method. Although a nonrespiration-resolved reconstruction requires 2 minutes, and therefore has been used *during* the session, the retrospective binning and reconstruction of three phases requires 15 minutes to reconstruct, which would have further prolonged the MR examination. Importantly, image acquisition times of 3 minutes and 24 seconds for the Tx-RPE-GRE and 6 minutes for the RPE-AFI are too long, particularly for future patient studies. With an increasing number of Tx channels,[44,45] the image acquisition needs to be accelerated to reduce total scan times, which could be achieved by decreasing the spatial resolution, increasing the undersampling factor, or introducing different k-space sampling strategies.[46] However, such steps might affect the quality of respiration-resolved B_1^+ maps. For brain studies, so-called universal pulses have been proposed,[6] which calculate pTx RF pulses based on training data sets in several subjects that are successfully applied to subjects not included in the training pool. Although applying this approach straightforwardly to the body might be challenging because of variable body sizes, this step, combined with a minimum of information on B_1^+ and/or anatomy of the present subject,[47] may achieve the desired result at a minimum of additional calibration time.

Therefore, the present work provides a valuable basis for performing 3D imaging of the human body without signal dropouts and lays the foundation for future developments necessary for body imaging at 7T.

ORCID
Sebastian Dietrich https://orcid.org/0000-0002-1610-909X
Christoph S. Aigner https://orcid.org/0000-0003-3618-9610
Christoph Kolbitsch https://orcid.org/0000-0002-4355-8368
Johannes Mayer https://orcid.org/0000-0002-2500-445X
Juliane Ludwig https://orcid.org/0000-0003-4042-8071
Simon Schmidt https://orcid.org/0000-0003-1835-4002
Tobias Schaeffter https://orcid.org/0000-0003-1310-2631
Sebastian Schmitter https://orcid.org/0000-0003-4410-6790

REFERENCES

1. Padormo F, Beqiri A, Hajnal JV, Malik SJ. Parallel transmission for ultrahigh-field imaging. *NMR Biomed*. 2016;29:1145-1161.

2. Ladd ME, Bachert P, Meyerspeer M, et al. Progress in nuclear magnetic resonance spectroscopy Pros and cons of ultra-high-field MRI/MRS for human application. *Prog Nucl Magn Reson Spectrosc*. 2018;109:1-50.

3. Erturk MA, Li X, Van De Moortele PF, Ugurbil K, Metzger GJ. Evolution of UHF Body imaging in the human torso at 7T: Technology, applications, and future directions. *Top Magn Reson Imaging*. 2019;28:101-124.

4. Metzger GJ, Snyder C, Akgun C, Vaughan T, Ugurbil K, Van De Moortele PF. Local B1+ shimming for prostate imaging with transceiver arrays at 7T based on subject-dependent transmit phase measurements. *Magn Reson Med*. 2008;59:396-409.

5. Wu X, Schmitter S, Auerbach EJ, Uğurbil K, Van de Moortele P-F. Mitigating transmit B1 inhomogeneity in the liver at 7T using multi-spoke parallel transmit RF pulse design. *Quant Imaging Med Surg*. 2014;4:4-10.

6. Gras V, Vignaud A, Amadon A, Le Bihan D, Boulant N. Universal pulses: A new concept for calibration-free parallel transmission. *Magn Reson Med*. 2017;77:635-643.

7. Sacolick LI, Wiesinger F, Hancu I, Vogel MW. B 1 mapping by Bloch-Siegert shift. *Magn Reson Med*. 2010;63:1315-1322.

8. Fautz H, Vogel M, Gross P. B1 mapping of coil arrays for parallel transmission. Proc. 16th Annu. Meet. ISMRM, Toronto, Canada: Abstract 1247; 2008.

9. Nehrke K, Börnert P. DREAM-a novel approach for robust, ultra-fast, multislice B1 mapping. *Magn Reson Med*. 2012;68:1517-1526.

10. Ehses P, Brenner D, Stirnberg R, Pracht ED, Stöcker T. Whole-brain B1-mapping using three-dimensional DREAM. *Magn Reson Med*. 2019;82:924-934.

11. Yarnykh VL. Actual flip-angle imaging in the pulsed steady state: A method for rapid three-dimensional mapping of the transmitted radiofrequency field. *Magn Reson Med*. 2007;57:192-200.

12. Van De Moortele P-F, Snyder C, Delabarre L, Adriany G, Vaughan T, Ugurbil K. Calibration tools for RF shim at very high field with multiple element RF coils: From ultra fast local relative phase to absolute magnitude B1+ mapping. Proc. 15th Annu. Meet. ISMRM, Berlin, Germany: Abstract 1676; 2007.

13. Brunheim S, Gratz M, Johst S, et al. Fast and accurate multi-channel B1+ mapping based on the TIAMO technique for 7T UHF body MRI. *Magn Reson Med*. 2018;79:2652-2664.

14. Van de Moortele P, Ugurbil K. Very fast multi channel B1 calibration at high field in the small flip angle regime. Proc. 17th Annu. Meet. ISMRM, Honolulu, Hawaii, USA: Abstract 367; 2009.

15. Metzger GJ, Auerbach EJ, Akgun C, et al. Dynamically applied B1+ shimming solutions for non-contrast enhanced renal angiography at 7.0 Tesla. *Magn Reson Med*. 2013;69:114-126.

16. Hess AT, Bissell MM, Ntusi NAB, et al. Aortic 4D flow: quantification of signal-to-noise ratio as a function of field strength and contrast enhancement for 1. 5T, 3T, and 7T. *Magn Reson Med*. 2015;73:1864-1871.

17. Schmitter S, Moeller S, Wu X, et al. Simultaneous multislice imaging in dynamic cardiac MRI at 7T using parallel transmission. *Magn Reson Med*. 2017;77:1010-1020.

18. He X, Ertürk MA, Grant A, et al. First in-vivo human imaging at 10.5T: Imaging the body at 447 MHz. *Magn Reson Med*. 2020;84:289-303.

19. Schmitter S, Adriany G, Waks M, et al. Bilateral multiband 4D flow MRI of the carotid arteries at 7T. *Magn Reson Med*. 2020;84:1947-1960.

20. Dietrich S, Aigner CS, Ludwig J, et al. Respiration-Resolved 3D Multi-Channel B1 mapping of the body at 7T. Proc. 28th Annu. Meet. ISMRM, Virtual Conference: Abstract 0660; 2020.

21. Cruz G, Atkinson D, Buerger C, Schaeffter T, Prieto C. Accelerated motion corrected three-dimensional abdominal MRI using total variation regularized SENSE reconstruction. *Magn Reson Med*. 2016;75:1484-1498.

22. Kolbitsch C. *Advanced Techniques for Cardiovascular Magnetic Resonance Imaging in Cases of Irregular Motion*, London: Ph.D. Thesis. King's College London, 2012.

23. Buerger C, Clough RE, King AP, Schaeffter T, Prieto C. Nonrigid motion modeling of the liver from 3-D undersampled self-gated golden-radial phase encoded MRI. *IEEE Trans Med Imaging*. 2012;31:805-815.

24. Dietrich S, Kolbitsch C, Schaeffter T, Schmitter S. 3D Radial Phase Encoded Flip Angle Imaging at Ultra-High Field Strength. Proc. 27th Annu. Meet. ISMRM, Montreal, Canada: Abstract 4560; 2019.

25. Prieto C, Uribe S, Razavi R, Atkinson D, Schaeffter T. 3D undersampled golden-radial phase encoding for DCE-MRA using inherently regularized iterative SENSE. *Magn Reson Med*. 2010;64:514-526.

26. Jackson JI, Meyer CH, Nishimura DG, Macovski A. Selection of a convolution function for Fourier inversion using gridding. *IEEE Trans Med Imaging*. 1991;10:473-478.

27. Pruessmann KP. Advances in sensitivity encoding with arbitrary k-space trajectories. *Magn Reson Med*. 2001;651:638-651.

28. Schmitter S, Wu X, Auerbach EJ, et al. Seven-Tesla time-of-flight angiography using a 16-channel parallel transmit system with power-constrained 3-dimensional spoke radiofrequency pulse design. *Invest Radiol*. 2014;49:314-325.

29. Rueckert D, Sonoda LI, Hayes C, Hill DLG, Leach MO, Hawkes DJ. Nonrigid registration using free-form deformations: Application to breast MR images. *IEEE Trans Med Imaging*. 1999;18:712-721.

30. Kolbitsch C, Bastkowski R, Schäffter T, et al. Respiratory motion corrected 4D flow using golden radial phase encoding. *Magn Reson Med*. 2020;83:635-644.

31. Van de Moortele P-F, Akgun C, Adriany G, et al. B1 destructive interferences and spatial phase patterns at 7 T with a head transceiver array coil. *Magn Reson Med*. 2005;54:1503-1518.

32. Suttie JJ, Delabarre L, Pitcher A, et al. 7 Tesla (T) human cardiovascular magnetic resonance imaging using FLASH and SSFP to assess cardiac function: Validation against 1.5T and 3T. *NMR Biomed*. 2012;25:27-34.

33. Setsompop K, Alagappan V, Gagoski B, et al. Slice-selective RF pulses for in vivo B1+ inhomogeneity mitigation at 7 Tesla using parallel RF excitation with a 16-element coil. *Magn Reson Med*. 2008;60:1422-1432.

34. Schmitter S, DelaBarre L, Wu X, et al. Cardiac imaging at 7 Tesla: Single- and two-spoke radiofrequency pulse design with 16-channel parallel excitation. *Magn Reson Med*. 2013;70:1210-1219.

35. Brunner DO, Pruessmann KP. B1+ interferometry for the calibration of RF transmitter arrays. *Magn Reson Med*. 2009;61:1480-1488.

36. Padormo F, Hess AT, Aljabar P, et al. Large dynamic range relative B1+ mapping. *Magn Reson Med*. 2016;76:490-499.

37. Orzada S, Maderwald S, Poser BA, Bitz AK, Quick HH, Ladd ME. RF excitation using time interleaved acquisition of modes (TIAMO) to address B1 inhomogeneity in high-field MRI. *Magn Reson Med*. 2010;64:327-333.

38. Nehrke K, Börnert P. Free-breathing abdominal B1 mapping at 3T using the DREAM approach. Proc. 20th Annu. Meet. ISMRM, Melbourne, Australia: 2012.

39. Rincón-Domínguez T, Menini A, Solana AB, et al. Accelerated multi-snapshot free-breathing B1+ mapping based on the dual refocusing echo acquisition mode technique (DREAM): An alternative to measure RF nonuniformity for cardiac MRI. *J Magn Reson Imaging*. 2019;49:499-507.

40. Föll D, Taeger S, Bode C, Jung B, Markl M. Age, gender, blood pressure, and ventricular geometry influence normal 3D blood flow characteristics in the left heart. *Eur Heart J Cardiovasc Imaging*. 2013;14:366-373.

41. Gosselin M-C, Neufeld E, Moser H, et al. Development of a new generation of high-resolution anatomical models for medical device evaluation: The Virtual Population 3.0. *Phys Med Biol*. 2014;59:5287-5303.

42. Hess AT, Jeaschke SHF, Chiew M. Click & run respiratory-resolved, ECG & navigator-free cardiac B0 & relative B1 calibration at 7T. ISMRM Work. Ultrah. F. Magn. Reson. Dubrovnik, Croatia: 2019.

43. Schmitter S, Wu X, Uğurbil K, Van de Moortele PF. Design of parallel transmission radiofrequency pulses robust against respiration in cardiac MRI at 7 Tesla. *Magn Reson Med*. 2015;74:1291-1305.

44. Orzada S, Solbach K, Gratz M, et al. A 32-channel parallel transmit system add-on for 7T MRI. *PLoS One*. 2019;14:1-20.

45. Ertürk MA, Raaijmakers AJE, Adriany G, Uğurbil K, Metzger GJ. A 16-channel combined loop-dipole transceiver array for 7 Tesla body MRI. *Magn Reson Med*. 2017;77:884-894.

46. Seiberlich N, Ehses P, Duerk J, Gilkeson R, Griswold M. Improved radial GRAPPA calibration for real-time free-breathing cardiac imaging. *Magn Reson Med*. 2011;65:492-505.

47. Ianni JD, Cao Z, Grissom WA. Machine learning RF shimming: Prediction by iteratively projected ridge regression. *Magn Reson Med*. 2018;80:1871-1881.

SUPPORTING INFORMATION

Additional Supporting Information may be found online in the Supporting Information section.

FIGURE S1 low impact on flip angle measurement in a strongly varying B_1^+ field is investigated with an agarose flow phantom. This phantom contains a pipe which is connected to a flow pump (CardioFlow 5000 MR, Shelley Medical Imaging Technologies, London, Canada) and driven with a constant flow. Shown are the resulting flip angle for a flow velocity of 0 cm/s (A) and 55 cm/s (B) and the corresponding gradient echo image (C), with a blue arrow indicating the flow direction. The relative difference RD of both measurements a and b is shown in (D), for an ROI covering the pipe a mean RD of 15% is calculated

FIGURE S2 Three different sets of B_1^+/ B_1^- maps were available for analysis: 32 Tx and 32 Rx fields, 8 Tx and 32 Rx fields, which corresponds to the setup used in this work, and 8 Tx and 8 Rx channels. For each of the three cases, we compared the sum of magnitude (SOM) across

the channels of simulated B_1^-, simulated B_1^+ and estimated B_1^+, which was obtained using Equation 3, with synthetic small flip angle gradient-echo-like images $I_{k,m} = B_k^+ * B_m^-$. The latter corresponds to the Tx-RPE-GRE acquisition. Deviations between the simulated B_1^+ and the resulting estimated B_1^+ maps are quantified by the relative difference RD of both(see Supporting Information Material M1). Resulting maps are shown for the central transversal slice through the heart are shown. Qualitatively the largest difference between the SOM is visible for the 8Tx/8Rx setup, with an increasing number of Tx and Rx channels the SOM maps become more homogenous which is also reflected in the relative difference B_1^+ maps. Quantitively the standard deviation of RD B_1^+ calculated for the whole thorax is 18% for 8Tx/8Rx, 10% for 8Tx/32Rx, and 5% for 32Tx/32Rx. Thus, using a 32Tx/32Rx coil setup would be ideal, but our system has only 8 Tx channels, and therefore, we had to use an 8Tx/32Rx configuration that still provides better results as compared to an 8Tx/8Rx set

FIGURE S3 Two representative time frames in three different views capturing systole and diastole of subject S8 are shown. Note that the same static phase-only shim Φ_{hom}, has been used for all three different orientations. Despite using the same shim setting, all three views are free of major B_1^+ related artifacts allowing to capture the whole heart movement. The corresponding cine GRE can be found in Supporting Information Video S1

FIGURE S4 Estimated, absolute B_1^+ maps of all the 11 subjects for all Tx channels are shown. Despite large variations in BMI (max/min: 34/19 kg/m²) the estimated, absolute B_1^+ maps are plausible and show no visible motion artifacts. Transversal slice of all 11 subjects with magnitude and phase for all eight Tx channels

VIDEO S1 Cine GRE of subject S8 in three different orientations with 1.3 mm in-plane resolution, 5mm slab, and 46 cardiac phases